



UNIVERSITY OF LEEDS

This is a repository copy of *Combustion Characteristics of Hydrogen, Propane and Methane Gases in a Boosted Featureless Port-Injection SI Engine*.

White Rose Research Online URL for this paper:

<https://eprints.whiterose.ac.uk/226909/>

Version: Accepted Version

Proceedings Paper:

Fakeye, A. and Yang, J. (2024) Combustion Characteristics of Hydrogen, Propane and Methane Gases in a Boosted Featureless Port-Injection SI Engine. In: Proceedings of the ASME 2024 ICE Forward Conference. ASME 2024 ICE Forward Conference, 20-23 Oct 2024, San Antonio, USA. The American Society of Mechanical Engineers (ASME)

<https://doi.org/10.1115/icef2024-148290>

Reuse

This article is distributed under the terms of the Creative Commons Attribution (CC BY) licence. This licence allows you to distribute, remix, tweak, and build upon the work, even commercially, as long as you credit the authors for the original work. More information and the full terms of the licence here:

<https://creativecommons.org/licenses/>

Takedown

If you consider content in White Rose Research Online to be in breach of UK law, please notify us by emailing eprints@whiterose.ac.uk including the URL of the record and the reason for the withdrawal request.



eprints@whiterose.ac.uk
<https://eprints.whiterose.ac.uk/>

DRAFT: ICEF2024-148290

Combustion Characteristics of Hydrogen, Propane and Methane Gases in a Boosted Featureless Port-Injection SI Engine

Adebayo Fakeye¹, Junfeng Yang¹

¹University of Leeds, Leeds, UK

ABSTRACT

The search for alternative transport fuel with comparable performance to fossil fuels in powering internal combustion engines (ICEs) has been a topical research project for decades. This is important because ICE is a well-developed technology, but fossil fuels are a finite resource, yet their consumption causes environmental damage. The alternative fuel is therefore expected to overcome these limitations. Hydrogen gas has been on top of the list as the most suitable option, but it is widely proposed dilute it with other fuels for better performance. To understand the effects of diluents such as methane and propane on the combustion characteristics hydrogen gas, Particle Image Velocimetry (PIV) was employed in this study to compare the fundamental combustion characteristics of hydrogen, propane and methane as single fuels at similar conditions in a featureless Leeds University Ported Optical Engine, (LUPOE-2D). The experiments were carried out at low speed of 50 rpm and a boosted inlet pressure of 1.67 bar at port inlet closing, typical of a downsized engine. The mixtures were ignited during the compression stroke at 5 bar. The inlet air was heated, and the temperature of the cylinder head was slightly adjusted from room temperature of $25 \pm 2^\circ\text{C}$ for the different mixtures such that a temperature of 439K was obtained for the mixtures at spark pressure of 5 bar. The temperature was estimated using the first law of thermodynamics. Flame combustion characteristics such as flame wrinkling parameters, stretch rate, burning velocities, etc., were derived and compared. There is good agreement between the stretched laminar burning velocities derived from direct measurement of the flame speed and unburned gas velocities ahead of the flame front, extrapolated to the zero-stretch, the values derived from the products of the unstretched flame speeds and the density ratios, and Chemkin-computed values. The burning rates increased with increase in flame stretch except for $H_2 \phi=0.5$ which increased to a peak before declining in similar manner as the flame stretch reached a peak and declined before the influence of wall confinement. The flame sphericity and the flame wrinkling amplitude were used to compare their

flame wrinkling characteristics of the flames. $H_2 \phi=0.5$ flames showed significant instability from the onset and became more wrinkled as the flame radius increased.

Keywords: burning velocity, flame wrinkling, SI engines, Particle Image Velocimetry

NOMENCLATURE

$u_{b,k}$	Burning velocity at crank angle k
$S_{n,k}$	Flame speed at crank angle
\bar{S}_n	Average of burning velocity over 18 sectors
$u_{g,k}$	Unburned gas velocity at crank angle k
\bar{u}_n	Average of burning velocity over 18 sectors
P_e	Perimeter of flame contour
ρ_u/ρ_b	Density ratio of unburned / burned gas
L_{ul}	Longitudinal integral length scale
L_{ut}	Transverse integral length scale
u_l	Laminar burning velocity
ϕ	Equivalence ratio
aTDC/bTDC	After/before Top Dead Center
u	Average velocity of the flow field
u'/u_{r-rms}	rms velocity / rms of radial velocity
ILS/Le	Integral Length Scale
μ	Dynamic viscosity of the premixture
ρ	Density of the premixtures
L	Integral length scale
u	Average velocity of the flow field

1. INTRODUCTION

The search for alternative transport fuel with comparable performance to fossil fuels in powering internal combustion engines (ICEs) has been a topical research project for decades. This is important because ICE is a well-developed technology, but fossil fuels are a finite resource and yet, their consumption causes environmental damage. Alternative fuel is expected to overcome these challenges. Despite several decades of research, a single sustainable fuel has not yet been conclusively agreed upon that satisfies the strict emissions regulations, especially for the more efficient boosted engines for transport vehicles. Road vehicles consume around 50% of the world's oil production [1]. This reportedly contributes more than 20% of the global

greenhouse gas emissions [2]. Hydrogen is commonly accepted as the best candidate as an alternative transport fuel largely for meeting the requirements for sustainable fuels and its unique combustion characteristics. Some of its beneficial combustion characteristics are nevertheless disadvantageous on another side. For example, its high resistance to auto-ignition greatly limits its use as a single fuel in compression ignition engines. This property is though, advantageous in preventing knock in spark ignition engines but it limits the operation range in compression ignition engines below the compression ratio of 29.1 [3]. Hydrogen blended with some hydrocarbon fuels have, however, shown several potentials, resultantly owing to the difference in response to flame stretch, heat/heat release rate and the laminar burning velocities.

These named parameters and the mixture Lewis number are the key parameters defining the combustion characteristics of the fuel blends [4]. Hence, diluents are widely proposed to achieve the best possible performance for hydrogen internal combustion engines (H₂-ICE). It was also observed that an optimal value exists for the hydrogen/hydrocarbon blend, which must be maintained to achieve the desired performance enhancement in ICEs. Two important findings are (i) there is a mixing threshold which depends largely on fossil fuels and (ii) there is significant changes in the combustion behaviors above the mixing threshold [1]. There is therefore a need to understand the comparative combustion characteristics of hydrogen and its diluents as single fuels at similar conditions.

The primary purpose of hydrogen dilution is control its propagation speed, avoid knocking and reduce NO_x emissions, especially at high engine loads [5]. Adding diluents to hydrogen changes the specie composition of the air-fuel mixtures and hence, influences heat and mass diffusion. This consequently alters the flame front structure of the flame. The appearance of cellular instability during the flame propagation wrinkles the flame front and induces turbulence in the unburned mixture, consequently leading to a sharp rise in the flame propagation speed. The cellular instability of premixed flames in ICEs can be caused by three basic phenomena: hydrodynamic or Darrieus-Landau (DL) instability, diffusive-thermal (DT) instability, and body-force instability [6]. Premixed H₂-air combustion in engine cylinder, especially at engine-like conditions, exhibits high laminar burning velocities such that the influence of buoyancy is effectively subdued. Thus, the effect of the density jumps across the flame front (hydrodynamic instability), and the competing effects between heat conduction from the flame and reactant diffusion toward the flame (diffusive-thermal instability) are the main causes of instabilities in hydrogen-powered ICEs. Several research have therefore attributed the principal mechanism of instabilities in H₂-ICE to hydrodynamic and thermos-diffusive instabilities giving rise to the onset of multi-dimensional cellular-shaped flames, aside from the system and chamber instabilities such as non-uniformity of flow and the body force.

[7] diluted hydrogen with acetylene, propane & methane in spherical bomb experiment using He-Ne laser shadowgraph system up to pressures of 7 bar. [8] employed Schlieren technique to measure the flame speeds for H₂/CH₄/air mixtures

for pure and diluted ratios of 30 %, 50 %, 70 methane at initial temperatures and pressures of 303 K and 360 K 0.1, 0.5 and 1.0 MPa for spherically expanding flames. Several other works have investigated the combustion phenomena of hydrogen but mostly at low pressures and temperatures [9][10][11], etc. Most of the work employed spherically expanding flames at low pressures, except [12] who employed high speed Schlieren imaging to study premixed hydrogen-air flames diluted with (He up to 65% & CO₂ up to 34%) up to 5 bar in a constant-pressure vessel. Whereas the operating regime of ICES comprise of cylindrical flames at high pressures and temperatures. This work therefore seeks to compare the combustion characteristics of high pressure premixed hydrogen, methane and propane at engine relevant condition and low turbulence. This will enhance understanding of the combustion phenomenon of hydrogen, methane and propane, their blends, and optimization in spark ignition engines. Particle Image Velocimetry (PIV) was employed to compare the flame propagation of the three fuels as single fuels under similar conditions at low speed. The PIV set comprises of the full-optical head Leeds University Ported Optical Engine, version 2, Disc-head (LUPOE-2D), a high-speed camera and a double cavity Nd-YLF laser. The low speed and disc-head version of the LUPOE engine setup was adopted to minimize the influence of turbulence on the effects of hydrodynamic and thermos-diffusive instabilities.

2. MATERIALS AND METHODS

The LUPOE-2D is a modified single-cylinder commercial Lister Petter-PH11 diesel engine. It employs a flat piston head with a two-inlet manifold diametrically at 20° to minimize turbulence. The optical head gives full access for recording the flame propagation in the engine cylinder. Table 1 shows the specifications of the LUPOE-2D. The speed of an induction electric motor (2880 rpm, 230 volts, 50 Hz) was controlled by adjusting the frequency of the supplied current using a FARA MOSCON-E5 inverter. The shaft of the induction motor was connected to the input shaft of a gearbox. The torque from the output shaft of the gearbox was transmitted to the crankshaft pulley of the LUPOE-2D engine. The reduction ratio of the gearbox was ten to one with ± 1% accuracy. This achieved operating the LUPOE engine at speed range of 10 to 200 rpm.

Table 1: Specification of LUPOE-2D

	Boosted Engine
Bore / Stroke / Effective stroke	80 / 110 / 72 mm
Clearance Height	7.5 mm
Clearance volume	37680 mm ³
Connecting-Rod Length	232 mm
Exhaust Port Open/Close (aTDC/bTDC)	127.6°
Inlet Port Open/Close (aTDC/bTDC)	107.8°
Geometric / Effective Compression Ratio	14.75 / 10.00

The recently modified LUPOE-2D is shown in Figure 1. 15% of the required air was seeded with olive oil using a TSI six-jet atomizer 9306A. The air recombined with the main flow and

injected into the inlet chamber 30cm upstream of the inlet port to obtain a homogeneous charge. Six rotameters were calibrated, two each for hydrogen, propane and methane to meter the fuels into the two inlet ports of the LUPOE Engine. The two symmetrically positioned inlet ports are slightly above the exhaust ports, hence a pressure of 1.67 bar was obtained at inlet ports closing. Some cycles were skipped from being ignited after a fired cycle to ensure the cylinder was free of residue gases and attained the required equivalence ratio without having to alter the inlet flow rate. The spark occurred at 5 bar and a temperature of 439k at spark timing of 28.6 bTDC. The temperature at the time of spark was obtained using the first law of thermodynamics and assuming isentropic compression. This was because the response time of the temperature transducer was insufficient to synchronize with the sampling rate of the pressure transducers.

The PIV set up consisted of a double cavity Nd-YLF laser machine, a LaVision flat-sheet optical generator, and high-speed controller, a FASTCAM SA1.1 high speed camera fitted with a filter lens, a timing unit, and a six-jet TSI seed generator. The flat sheet generator was used to generate a flat sheet of about 1mm thickness from the laser light to illuminate the seeded fuel-air mixture (seeded with olive oil) in the combustion chamber. The High-speed camera was used to capture the light scattered by the trace particles in the unburned gas region. DaVis 8 software was used to record double frames images of the propagating flames at camera frame rate of 5 kHz, 512 x 512 resolution. Pulse interval (dt) of 20μs and 50μs, were used for of H₂ φ=1.0 and C₃H₈ φ=1.0 respectively while 75μs was used for CH₄ φ=1.0 and H₂ φ=0.5 respectively. DaVis8 was also used to produce the velocity vectors and were further processed by MATLAB codes. Figure 2 shows the schematic of the PIV control and data acquisition system. To maintain a laminar flow in the engine cylinder and to eliminate the influence of turbulence on the flame propagation, the LUPOE engine was operated at low speed 50 rpm. The flow in the LUPOE engine has been found to be locally isotropic and homogenous [13][14]. The velocity, V, the rms of the velocity, u', and the integral length scales derived from motored cycles were similar for all the conditions. The velocity and its rms are both 0.2m/s. The length scales were less than 6mm. Hence, the Reynold's numbers for all the cases, derived using equation (1), was found to be less than 230 for all the cases and located in the corrugated flamelet region in the Borghi diagram.

$$Re = \frac{\rho u L}{\mu}, \quad (1)$$

where μ and ρ are the dynamic viscosity and density of the premixtures, L is the integral length scale and u is the average velocity of the flow field. The transverse and longitudinal correlations functions of the velocity u , $R_{ux}(r)$ and $R_{uy}(r)$ with respect to correlation distance r are given in equations 2 and 3 respectively.

$$R_{ux}(x, y, r) = \frac{\frac{1}{N} \sum_{i=1}^N (u(x, y, i) u(x+r, y, i))}{u'(x, y) u'(x+r, y)} \quad (2)$$

$$R_{uy}(x, y, r) = \frac{\frac{1}{N} \sum_{i=1}^N (u(x, y, i) u(x, y+r, i))}{u'(x, y) u'(x, y+r)} \quad (3)$$

The longitudinal and transverse Integral Length Scales are thus estimated from equations 5 and 6.

$$L_{ul} = \int_0^{r1} R_{ux}(x, y, r) dr \quad (4)$$

$$L_{ut} = \int_0^{r1} R_{uy}(x, y, r) dr \quad (5)$$

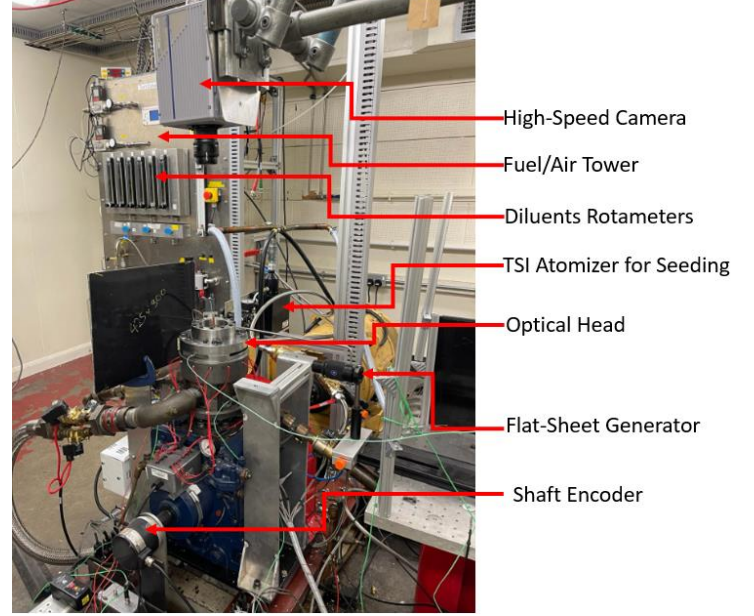


FIGURE 1: Modified LUPOE-2D and the air/ fuel supply tower

$r1$ and $r2$ are the first r values in the correlation functions where the values of $R_{ux}(x, y, r1)$ and $R_{uy}(x, y, r2)$ equals zero.

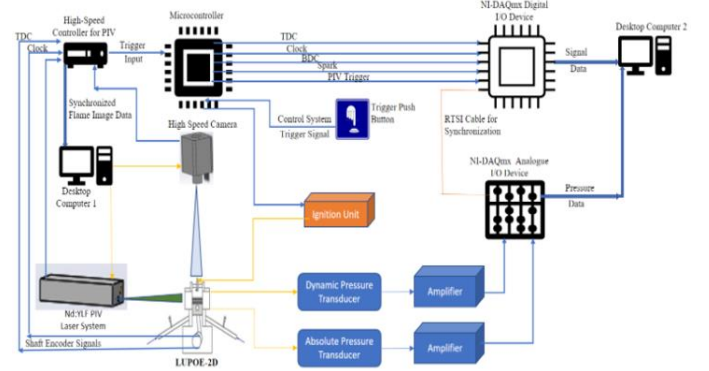


FIGURE 2: Schematic of the PIV Control & Data Acquisition System

2.1 Image Processing

The binarization procedure of [15] was employed to generate the flame contours. Adaptive thresholding with low pass filter was used to generate a threshold map for the image binarization. The black portion of the binarized images are the flame sections while the white parts are the unburned gas regions. A Wiener filter was applied to the binarized image to eliminate noise. An edge function in MATLAB was used to extract the edges of the

black sections of the binarized images to produce the final flame contours as shown in Fig. 3. The thin centrally positioned spark plug and the wall reflection were masked out in the flame images processing.

Flame Speed Derivation: A LaVision High-Speed Controller was employed to synchronize the LUPOE engine, the camera and the Laser illumination. DaVis software that was used to record synchronized images of the flame propagation was also used to derive the velocity vectors. The evolution of the flame contours shown in Figure 3 was used to derive the flame speed using equation 2. It also shows the sectioning of the flame into 36 equal sectors, the flame speed superimposed on the upper 18 sectors, and a sample of the velocity vectors output from DaVis. The upper half of the flame was assumed symmetrical with the lower half; only the upper 18 sectors facing incoming laser light were used for analyzing the burning velocities. This was necessary because deflection of the flash sheet laser light introduced errors in the other half of the flame vectors. The flame speed at each sector was estimated from equation 6. Equation 7 was used to derive the mean flame speed of the upper 18. Equation 8 is used to derive the flame stretch for the cylindrical laminar flames.

$$S_n = \frac{d}{t_2 - t_1} \frac{m}{s} \quad (6)$$

$$\bar{S}_n(t) = \frac{1}{n} \sum_{k=1}^n S_{n_k}(t) \quad (7)$$

$$\text{Flame Stretch} = \frac{\text{Average Speed}}{\text{Average Radius}} \frac{1}{s} \quad (8)$$

The flames also exhibited different degrees of light reflection. Propane with equivalence ratio $\phi=1.0$ exhibited more light reflection towards the end of combustion. Therefore, the velocity vectors of propane beyond the radius of 25mm were overestimated, hence, ignored.

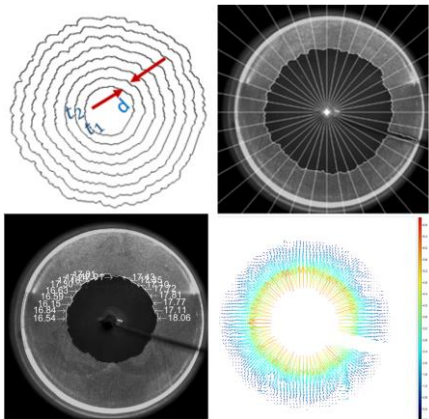


FIGURE 3: Flame edge detection procedure/Velocity Field

Burning Velocity Derivation: DaVis software was used for recording the flame images and deriving the velocity vectors-sample shown in Fig.3. The upper 18 sectors unaffected by laser reflection were divided into annular of 3 or 4 pixels, depending

on the degree of wrinkling of the flame contours. The velocity vectors generated in Cartesian form from the DaVis image processing were resolved into polar coordinates along the direction of the radial flame propagation. Since the flame propagates perpendicularly to the flame front, the position of the spark plug was used as the center of the flame to obtain the radial and tangential components of the flow field from the velocity vectors.

The velocities of the unburned gas, $u_{g,k}$, at the flame edge for the four cases were obtained by a polynomial function fitting the behavior of radial velocity vectors for each premixture considered [16] using OriginPro 2023b. The burning velocities in each sector were, $u_{b,k}$, hence, evaluated according to equation 9. This was averaged over the 18 sectors to obtain the burning velocities using equation 10.

$$u_{b,k} = S_{n,k} - u_{g,k} \quad (9)$$

$$\bar{u}_n(t) = \frac{1}{n} \sum_{k=1}^n u_{b_k}(t) \quad (10)$$

where $S_{n,k}$ and $u_{g,k}$ are the flame speed and unburned gas velocity at each sector for the crank angles. Since isometry of the upper and lower halves were assumed, the Sphericity was calculated using equation 11.

$$\text{Sphericity} = \frac{4\pi A}{P_e^2} \quad (11)$$

where A is the area of the upper half of the measured laser sheet flame and P_e is the perimeter of the flame contour. Typically, sphericity of 1.0 implies no wrinkling whereas wrinkled flame front has more surface area with larger perimeter, hence lower Sphericity.

3. RESULTS AND DISCUSSION

The rates of flame propagation of the four conditions investigated are shown in Fig. 4. The figure shows that hydrogen $\phi=1.0$ propagates much faster than the rest, followed by propane, methane and lastly, hydrogen $\phi=0.5$. So, are their stretch rates in similar sequence shown in Fig. 5. In Fig. 6, at least four cycles were used to derive the flame speed for each of the cases. Fig. 7 shows the estimation of the unstretched flame speeds from the stretch flames for the four cases. The results are shown in Table 2.

Table 2: Flame Speeds & Burning Velocities [m/s]

Fuel	ρ_b/ρ_u	$s_n \times \rho_b/\rho_u$	u_l	Chemkin Computation
H ₂ $\phi=1.0$	0.203	3.693	3.220	3.760
C ₃ H ₈ $\phi=1.0$	0.176	0.683	0.553	0.595
CH ₄ $\phi=1.0$	0.187	0.505	0.382	0.390
H ₂ $\phi=0.5$	0.273	0.847	0.510	0.560

Extrapolation Methods: It has been established that the region between the flame radii of 10mm and 20mm for the LUPOE engine is unaffected by the spark energy and free from the wall confinement influence [17][15]. As shown in Fig. 7, the quasi-

stable, fully developed flame region within the flame radii of 10mm and 20mm was used for the evaluation of the unstretched flame speeds. Linear extrapolation was used to derive zero-stretch flame speeds [18][19]. Fast flame propagation speed of H_2 $\phi=1.0$ resulted to a low number of measured points. The stretched burning velocities obtained from the flame speed minus the unburned gas velocity were also extrapolated to the zero-stretch using the similar stable region.

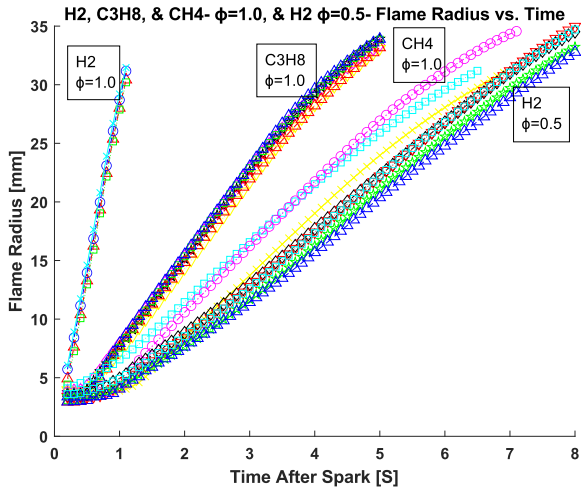


FIGURE 4: Flame Radius vs. Time after Spark

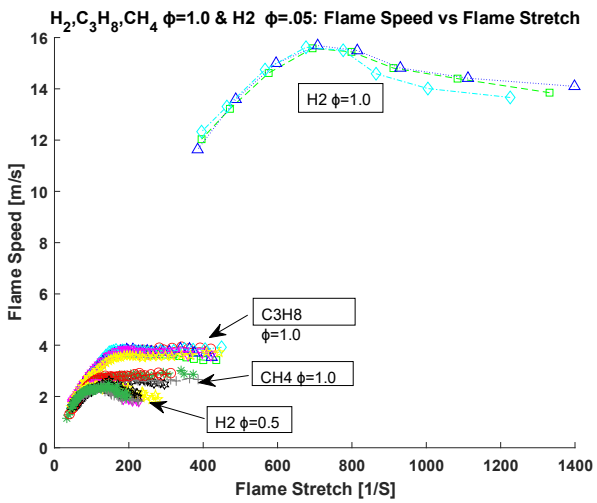
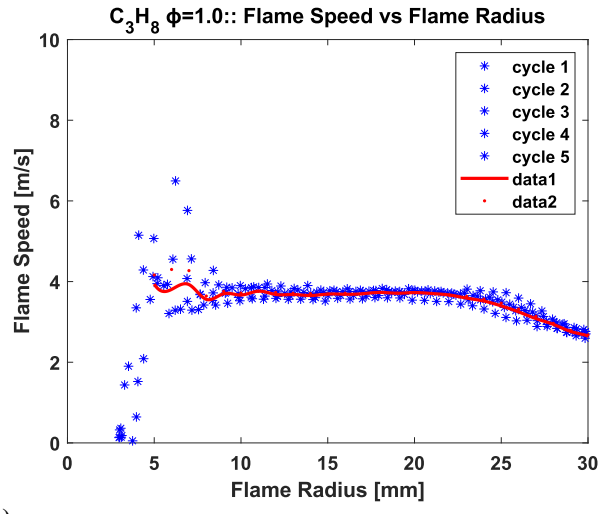
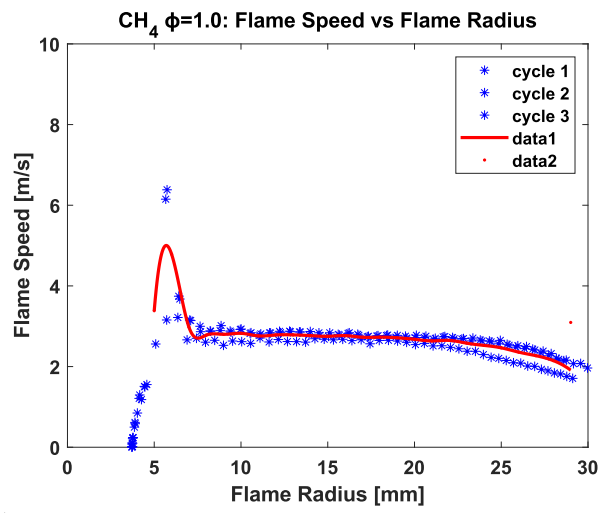


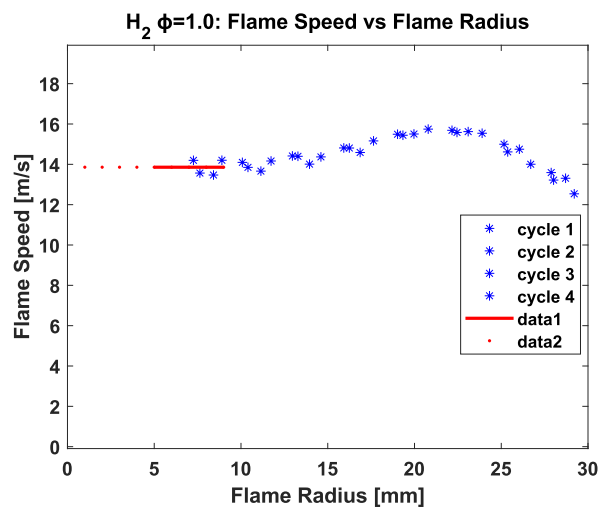
FIGURE 5: Flame Speed vs. Flame Stretch



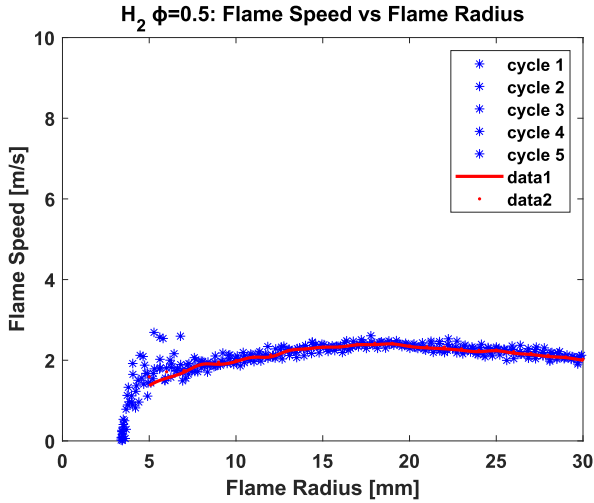
(a)



(b)



(c)



(d)
FIGURE 6: Flame Speed vs. Flame Radius

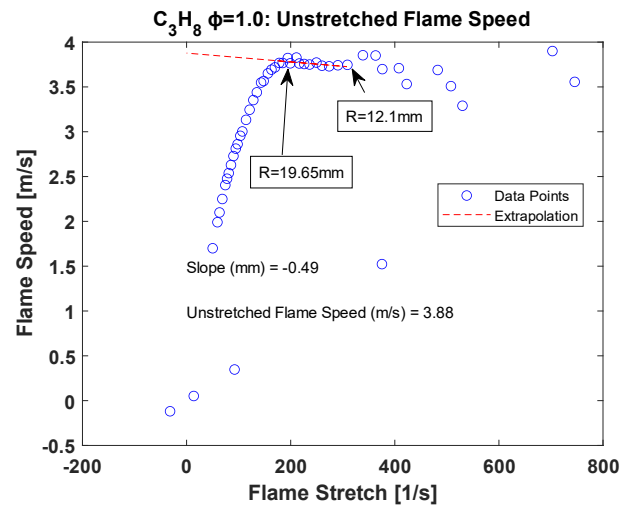
It can be observed from Fig. 8 that a linear relationship reasonable defines the experimental data within the indicated flame radii of 10 and 20 mm except for $H_2 \phi=0.5$ where third order polynomial fits the data set from flame radius 5 mm to 35 mm to obtain unstretched laminar burning velocity of 0.51m/s. The burning velocities of the smooth-edged flames increase with increase in flame stretch along the radial direction. Like the stretch rate profile of $H_2 \phi=0.5$, the burning velocity of $H_2 \phi=0.5$, which shows more wrinkled flame contours, increases with increase in flame stretch to a peak before declining (Fig. 8). This is attributed to the influence of Soret diffusion on H_2 molecules at $\phi=0.5$ compared to other cases with equivalence ratios $\phi=1.0$. [20] numerically investigated the effect of Soret diffusion on lean premixed H_2 flames and established the influence of the flame stretch, pressure and temperature on the flame speed and burning velocity characteristics. Increased pressure enhances the Soret diffusion of H_2 on the global consumption speed. As seen from Fig. 8, and in agreement with [20], Soret diffusion affects the flame propagation more in the early stage of the flame propagation than in the later stage (before the influence of cylinder walls) due to the local enrichment of H_2 resulting from flame curvature effects.

Fig. 8 describes the derivation of the laminar burning velocities from the stretched flames. The results are also shown in Table 2. The estimation of the burning velocities as the product of the unstretched flame speeds and the density ratio of the premixtures are shown in Table 2. The density ratios of the fuels were obtained from GASEQ and are listed on Table 2. The laminar burning velocities obtained from Chemkin simulations for the experimental conditions are as well, presented in Table 2.

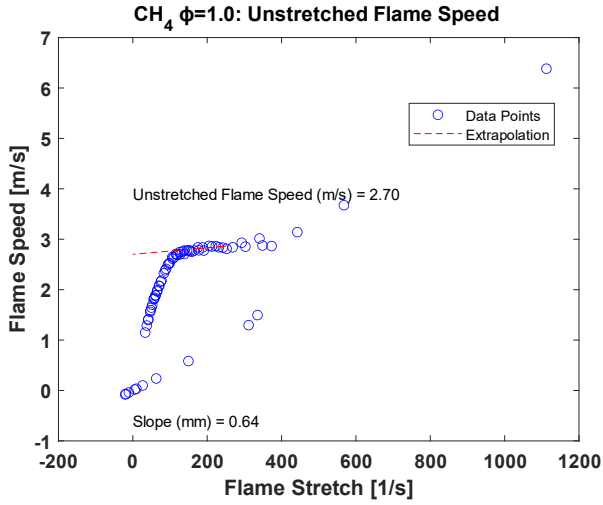
Fig. 9(a-d) show the graphs of the flame speed S_t , unburned gas velocity u_g , the stretched burning velocities u_b , and the rms of the velocity rms Vel, and the radial velocity u_{r-rms} for a representative cycle for the four cases. The influence of the developing flame on the speed of unburned gas ahead of the flame can be noted from the rms of the velocity and the radial

velocity ahead of the flame front. From the plots of the rms Vel and u_{r-rms} , $H_2 \phi=1.0$ has the highest influence on the unburned gas ahead of the flame while $H_2 \phi=1.0$ has the least. The higher the flame speed, the higher the turbulence ahead of the flame. The burning velocities derived from direct PIV measurements (Fig. 8), (Fig. A6, Appendix) are considerable close to the values derived from Chemkin and from the indirect method (Fig. 7). $CH_4 \phi=1.0$ has a discrepancy of 29.5% from the Chemkin-derived value while $H_2 \phi=0.5$ has 51.25%. Several sources of uncertainties affect the measurement of laminar burning velocities. However, it can be noted from Table 2 that the closeness of the values obtained from the indirect method to the Chemkin-derived values varies from $H_2 \phi=1.0$ which has the fastest flames speed (and hence the combustion occurred nearly constant volume) to the least, $H_2 \phi=0.5$. The assumption of constant volume combustion influences the accuracy of the density ratio, hence the product $S_n \times \rho_b / \rho_u$.

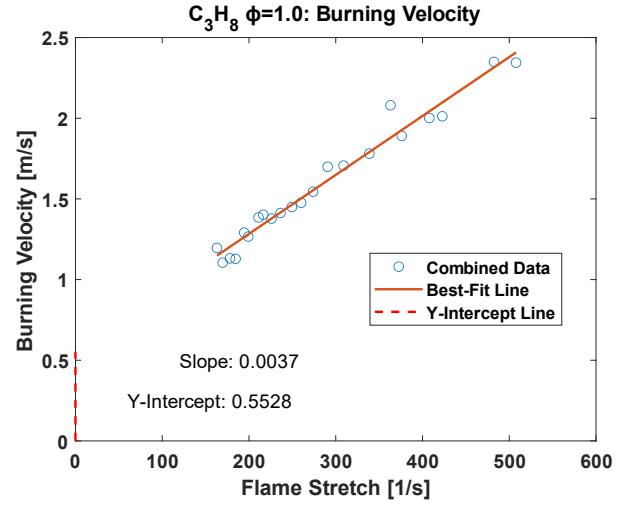
Fig. 10 compares the sphericity of the gases derived from four cycles for each. The figure shows that $H_2 \phi=0.5$ is increasingly wrinkled as the flame grows unlike others. The plot of the flame sphericity (Fig. 10) shows that $H_2 \phi=1.0$ shows the highest Sphericity, implying the less wrinkled flame. However, $CH_4 \phi=1.0$ shows constant Sphericity of 0.42 throughout the combustion excluding the regions influenced by ignition energy and wall confinement. Figures 11 (others in Fig. A1 in the Appendix) and 12 that there are big curvatures on the flame contours of $CH_4 \phi=1.0$ and $C_3H_8 \phi=1.0$. This trend is observed in their flame images right from the early flame development stage (above 7mm flame radius) and may be caused by the interaction between the flame and the shape of the spark at the flame initiation stage.



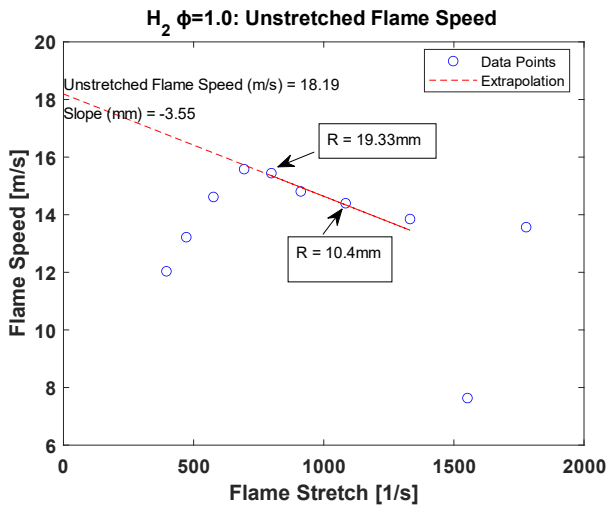
(a)



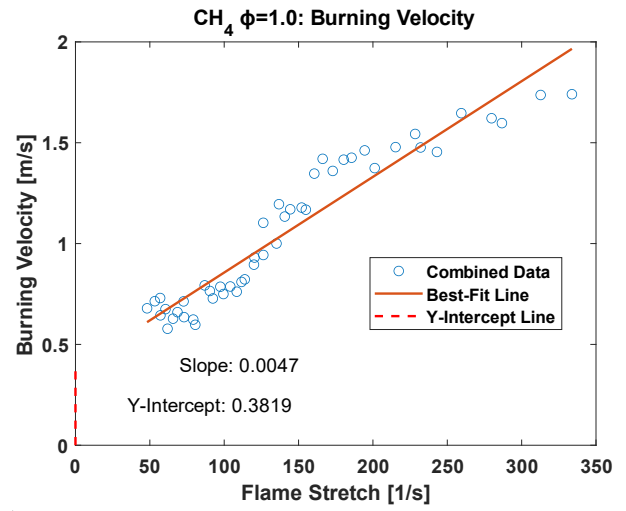
(b)



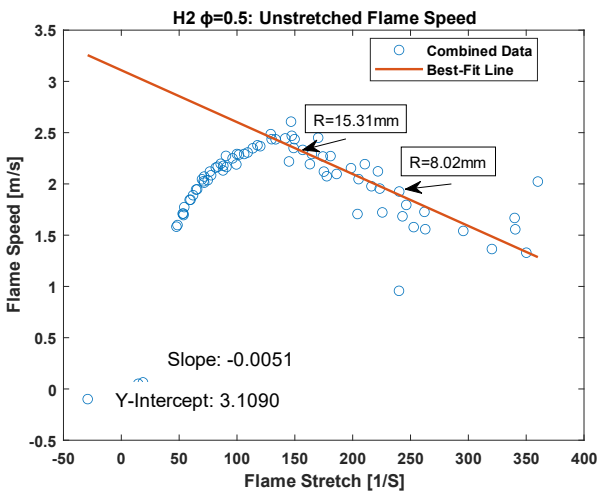
(a)



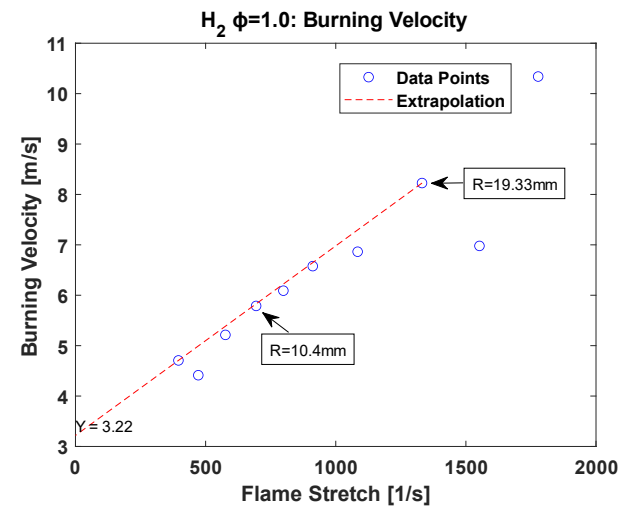
(c)



(b)

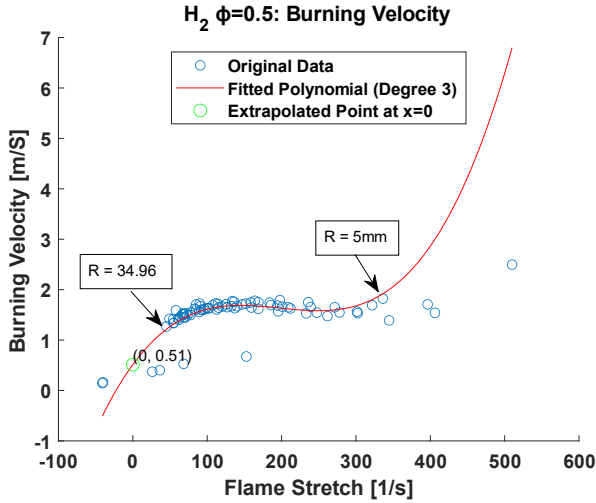


(d)



(c)

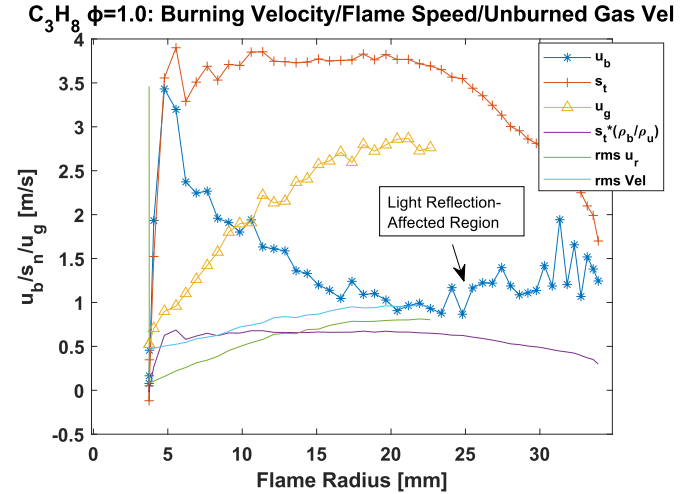
FIGURE 7: Estimation of Unstretched Flame Speeds



(d) **FIGURE 8:** Estimation of Laminar Burning Velocities

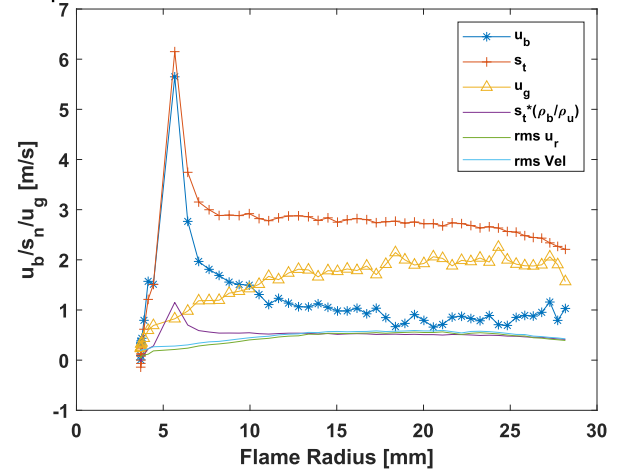
The flame sphericity and flame wrinkling amplitude were used to compare their flame wrinkling behaviours. Fig. 10 shows the plot of the flame sphericity for the flames. $H_2 \phi=1.0$ and $H_2 \phi=0.5$ flames have the highest Sphericity of 0.64 at flame radius of 6.58 while of $C_3H_8 \phi=1.0$ and $CH_4 \phi=1.0$ have respectively have 0.40 and 0.47 at the referenced radius. However, the Sphericity of $H_2 \phi=0.5$ flame unsteadily declines to the least at 28mm radius. This shows $H_2 \phi=0.5$ flame is unstable from the onset and could not maintain any stable Sphericity region, unlike other cases with $\phi=1.0$. The sphericity $H_2 \phi=1.0$ steadily decreased from 0.65 at flame radius $r = 7.5\text{mm}$ to 0.52 at $r = 18.77\text{mm}$ and remained constant up to 25.18 mm flame radius. The sphericity of $C_3H_8 \phi=1.0$ steadily decreased from 0.49 at $r = 8.44\text{ mm}$ to 0.36 at $r = 22.4\text{mm}$ and remained constant to 30 mm flame radius. The sphericity of $CH_4 \phi=1.0$ steadily but sharply declined from 0.53 at $r = 5.56\text{ mm}$ to 0.41 at $r = 8.38$ and remained constant up to flame radius = 25 mm, implying that $CH_4 \phi=1.0$ was not subjected to more flame wrinkling in the fully developed region other than at the initial stage of combustion. Sphericity of $H_2 \phi=1.0$ declined from 0.64 at $r=6.5$ at first to 0.53 at first at flame radius 18 mm, maintained a stably Sphericity region up to 26 mm radius before steadily declining again to 0.35 at flame radius 27.89 mm.

The integral length scale (ILS) of wrinkle averaged over four cycles is shown in Fig. 14. The ILS of wrinkle is quite similar for all the cases except $H_2 \phi=1.0$ which shows a distinctively high ILS from the others.



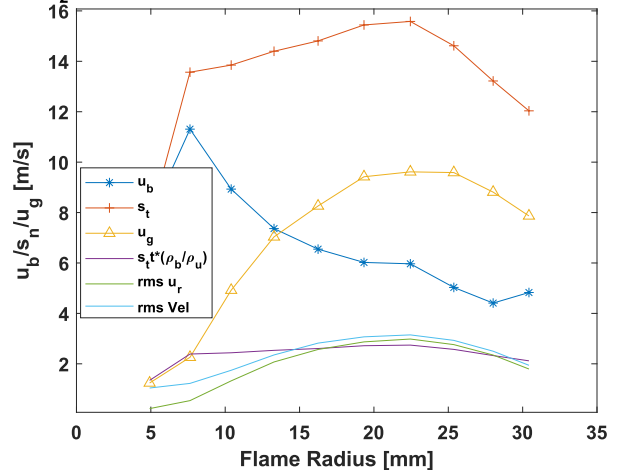
(a)

CH₄ $\phi=1.0$: Burning Velocity/Flame Speed/Unburned Gas Vel

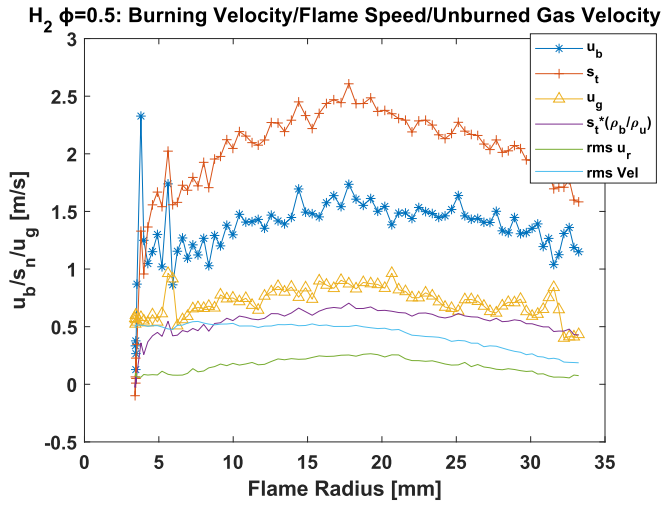


(b)

H₂ $\phi=1.0$: Burning Velocity/Flame Speed/Unburned Gas Vel



(c)



(d)

FIGURE 9: Flame Speed/Burning Velocities/Gas Velocities etc. vs Flame Radius

The data for the flame speeds RMS in the 18 sectors at flame initiation stage could not be captured for $H_2 \phi=1$ because of its high flame speed. It was observed that $CH_4 \phi=1.0$ has a more stable pattern from the flame initiation to the fully developed stage (Fig A3, Appendix). The integral length scales are similar for all the cases (Fig 13).

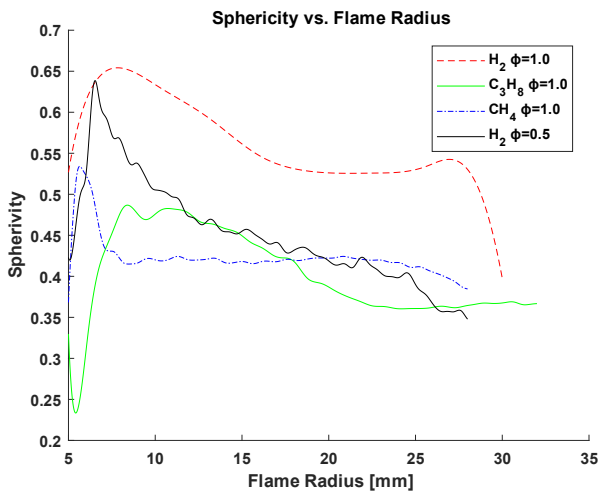


FIGURE 10: Flame Sphericity (Averaged from 4 cycles each)

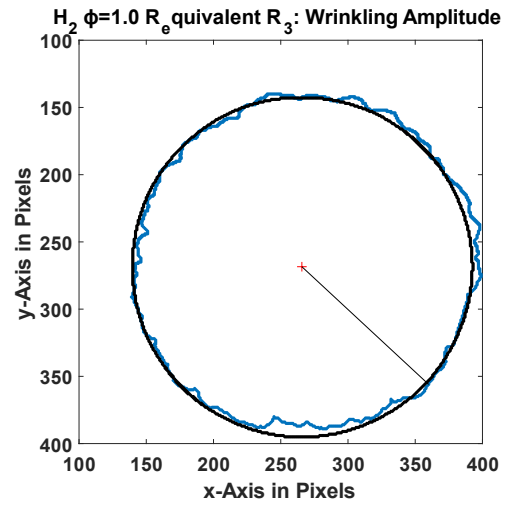
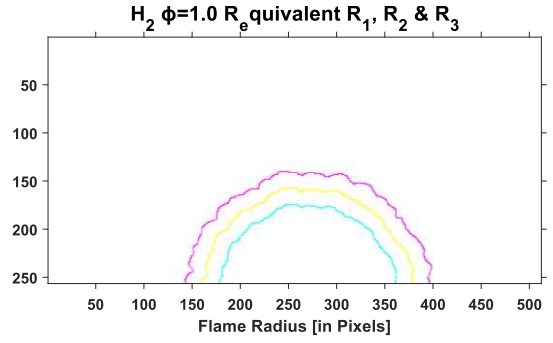
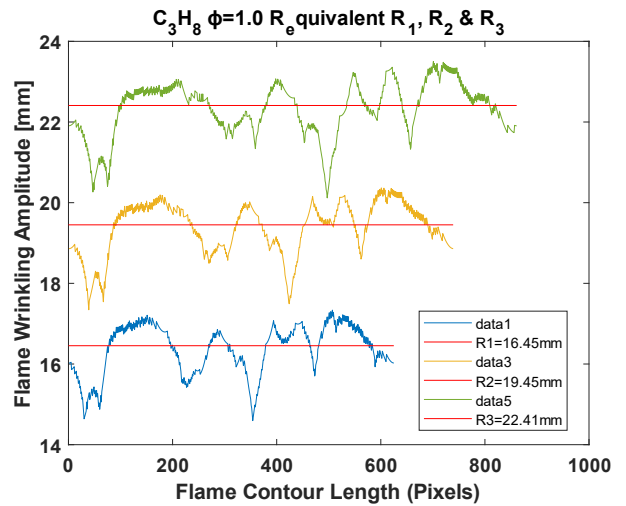
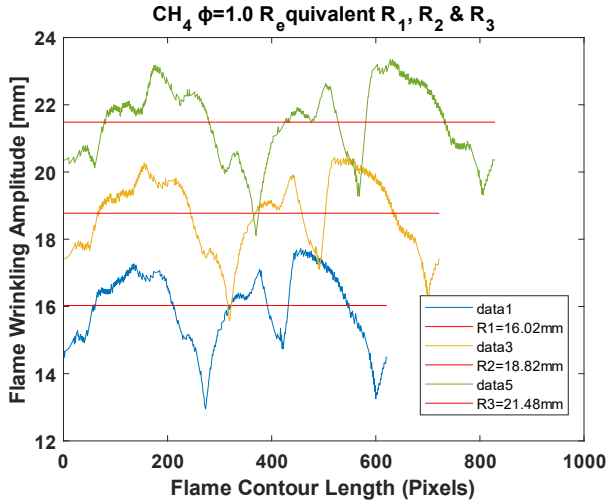


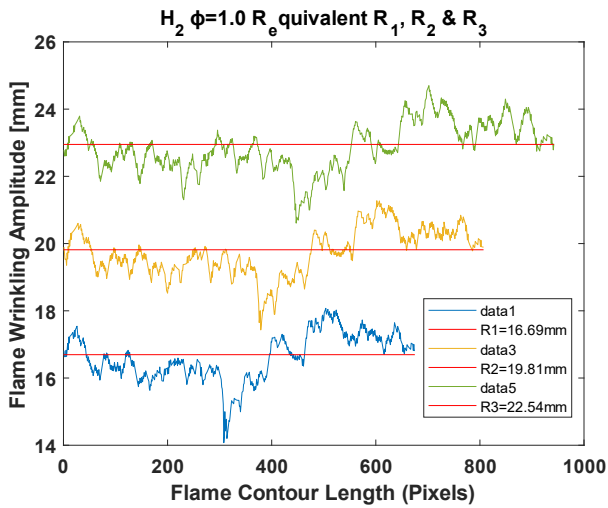
FIGURE 11: Flame Contours & Wrinkling Diagram: $H_2 \phi=1.0$



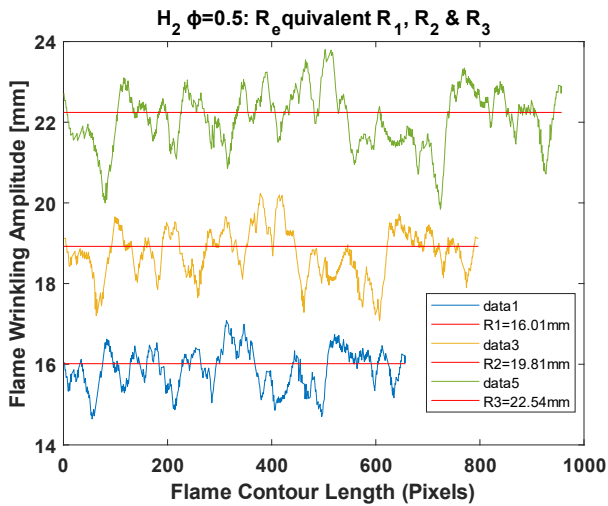
(a)



(b)



(c)



(d)

FIGURE 12: Flame Wrinkling Amplitude

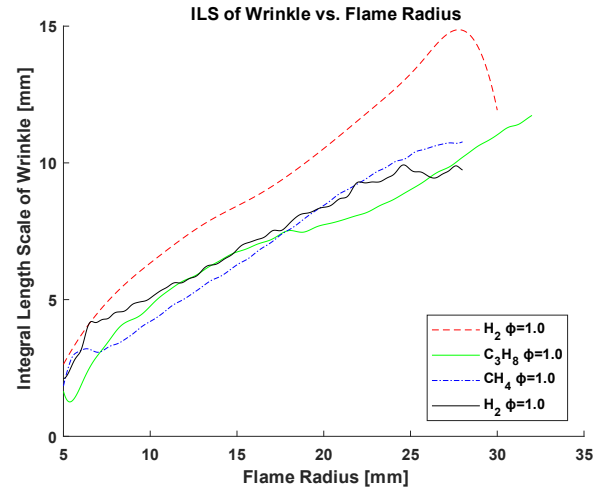


FIGURE 13: ILS of Wrinkle (Averaged over 4 cycles each)

Effect of Instability: The local curvatures and stretch effect on $H_2 \phi=0.5$ flames increases the local flame speeds in proportion to the cellular flame surface area [21][22][23]. Hence, the burning velocity obtained from direct measurement of the local flame speed minus the unburned gas velocity is close to the one obtained from Chemkin-computed value. For the low turbulence flow, and $H_2 \phi=0.5$ having a Lewis number of 0.376 (obtained from Chemkin), the molecular diffusivity of hydrogen is more than the thermal energy conducted away by the low turbulence flow. More chemical energy is transported towards the flame front thereby increasing the local mixture richness at the cellular flame front. This increases the local flame speed, and hence the burning velocity at the flame front.

4. CONCLUSION

The combustion characteristics of hydrogen, propane and methane have been compared using cylindrical flame propagation in an optical ICE. There is good agreement between the results obtained from direct measurement, indirect measurement and the Chemkin obtained values of the laminar burning velocities. The overestimation of the values obtained for $H_2 \phi=0.5$ and $CH_4 \phi=1.0$ from the indirect measurement is attributed to their relatively low speeds which assumed constant volume combustion for the combustion that occurred over 4 crank angle degrees compare to $H_2 \phi=1.0$ and $C_3H_8 \phi=1.0$ which occurred over much less crank angle degrees. The $H_2 \phi=0.5$ flames showed significant flame wrinkling from the onset. The flame wrinkling was noticed to increase as the flame propagated, unlike hydrogen, propane, and methane, at equivalence ratio $\phi=1.0$. It was observed that high/low flame speeds resulted in high/low turbulence ahead of the flame front. The burning rates increased with the flame stretch for all cases except for $H_2 \phi=0.5$, which increased to a peak at 150 s^{-1} before declining. This trend agrees with literature. $H_2 \phi=1.0$ flame has the highest sphericity, implying that it is the least wrinkled flame.

ACKNOWLEDGEMENTS

We thank EPSRC (Grant No. EP/W002299/1) for the financial support. Mr. Adebayo Fakeye appreciates the support he received from TETFund. The contributions of the following people are also acknowledged: Jeon Do Kim, Peter Zhang, Junior Achumu, Mohamed Morsy, Sam Flint, Peter Grieve and Max Pepper

REFERENCES

- [1] S. Ehsan Hosseini and B. Butler, "International Journal of Green Energy An overview of development and challenges in hydrogen powered vehicles An overview of development and challenges in hydrogen powered vehicles," 2019, doi: 10.1080/15435075.2019.1685999.
- [2] B. Saboori, M. Sapri, and M. bin Baba, "Economic growth, energy consumption and CO₂ emissions in OECD (Organization for Economic Co-operation and Development)'s transport sector: A fully modified bi-directional relationship approach," *Energy*, vol. 66, pp. 150–161, 2014, doi: 10.1016/j.energy.2013.12.048.
- [3] P. Dimitriou and T. Tsujimura, "A review of hydrogen as a compression ignition engine fuel," *Int. J. Hydrogen Energy*, vol. 42, no. 38, pp. 24470–24486, 2017, doi: 10.1016/j.ijhydene.2017.07.232.
- [4] P. Brequigny, F. Halter, and C. Mounaïm-Rousselle, "Lewis number and Markstein length effects on turbulent expanding flames in a spherical vessel," *Exp. Therm. Fluid Sci.*, vol. 73, pp. 33–41, 2016, doi: 10.1016/j.expthermflusci.2015.08.021.
- [5] C. M. White, R. R. Steeper, and A. E. Lutz, "The hydrogen-fueled internal combustion engine: a technical review," *Int. J. Hydrogen Energy*, vol. 31, no. 10, pp. 1292–1305, 2006, doi: 10.1016/j.ijhydene.2005.12.001.
- [6] H. M. Li, G. X. Li, Z. Y. Sun, Y. Zhai, and Z. H. Zhou, "Research on cellular instabilities of lean premixed syngas flames under various hydrogen fractions using a constant volume vessel," *Energies*, vol. 7, no. 7, pp. 4710–4726, 2014, doi: 10.3390/en7074710.
- [7] B. E. Milton and J. C. Keck, "Laminar burning velocities in stoichiometric hydrogen and hydrogenhydrocarbon gas mixtures," *Combust. Flame*, vol. 58, no. 1, pp. 13–22, 1984, doi: 10.1016/0010-2180(84)90074-9.
- [8] M. AL-Khafaji *et al.*, "Laminar burning velocities and Markstein numbers for pure hydrogen and methane/hydrogen/air mixtures at elevated pressures," *Fuel*, vol. 354, no. August, 2023, doi: 10.1016/j.fuel.2023.129331.
- [9] V. A. Alekseev, M. Christensen, E. Berrocal, E. J. K. Nilsson, and A. A. Konnov, "Laminar premixed flat non-stretched lean flames of hydrogen in air," *Combust. Flame*, vol. 162, no. 10, pp. 4063–4074, 2015, doi: 10.1016/j.combustflame.2015.07.045.
- [10] J. Pareja, H. J. Burbano, A. Amell, and J. Carvajal, "Laminar burning velocities and flame stability analysis of hydrogen/air premixed flames at low pressure," *Int. J. Hydrogen Energy*, vol. 36, no. 10, pp. 6317–6324, 2011, doi: 10.1016/j.ijhydene.2011.02.042.
- [11] E. Varea, J. Beeckmann, H. Pitsch, Z. Chen, and B. Renou, "Determination of burning velocities from spherically expanding H₂/air flames," *Proc. Combust. Inst.*, vol. 35, no. 1, pp. 711–719, 2015, doi: 10.1016/j.proci.2014.05.137.
- [12] S. Yang, X. Yang, F. Wu, Y. Ju, and C. K. Law, "Laminar flame speeds and kinetic modeling of H₂/O₂/diluent mixtures at sub-atmospheric and elevated pressures," *Proc. Combust. Inst.*, vol. 36, no. 1, pp. 491–498, 2017, doi: 10.1016/j.proci.2016.06.122.
- [13] A. A. Burluka, A. M. T. A. El-Dein Hussin, Z. Y. Ling, and C. G. W. Sheppard, "Effects of large-scale turbulence on cyclic variability in spark-ignition engine," *Exp. Therm. Fluid Sci.*, vol. 43, pp. 13–22, 2012, doi: 10.1016/j.expthermflusci.2012.04.012.
- [14] Z. Ling, "Flame propagation and autoignition in a high pressure optical engine," *Ph.D. Thesis*, no. September, 2014, [Online]. Available: <https://ru.idm.oclc.org/login?url=https://search.proquest.com/docview/1827468906?accountid=11795%0Ahttp://ru.on.worldcat.org/atoztitles/link?sid=ProQ:&issn=&v volume=&issue=&title=Flame+propagation+and+autoignition+in+a+high+pressure+optical+engine&spage=&d>
- [15] W. Zhang, M. E. Morsy, Z. Ling, and J. Yang, "Characterization of flame front wrinkling in a highly pressure-charged spark ignition engine," *Exp. Therm. Fluid Sci.*, vol. 132, no. November 2021, p. 110534, 2022, doi: 10.1016/j.expthermflusci.2021.110534.
- [16] V. Acharya *et al.*, "Velocity and flame wrinkling characteristics of a transversely forced, bluff-body stabilized flame, Part II: Flame response modeling and comparison with measurements," *Combust. Sci. Technol.*, vol. 185, no. 7, pp. 1077–1097, 2013, doi: 10.1080/00102202.2013.777715.
- [17] C. M. Beng and P. Thesis, "Laminar and Turbulent Burning Characteristics of Hydrocarbon Fuels Title: Laminar and Turbulent Burning Characteristics of Hydrocarbon Fuels," no. August, 2008.
- [18] C. K. Law, "Dynamics of stretched flames," *Symp. Combust.*, vol. 22, no. 1, pp. 1381–1402, 1989, doi: 10.1016/S0082-0784(89)80149-3.
- [19] S. Balusamy, a Cessou, and B. Lecordier, "Measurement of laminar burning velocity—A new PIV approach," *4th Eur. Combust. Meet. Vienna*, no. 3, pp. 1–6, 2009, [Online]. Available: http://combustion.org.uk/ECM_2009/P810161.pdf
- [20] Z. Zhou, F. E. Hernández-Pérez, Y. Shoshin, J. A. van Oijen, and L. P. H. de Goeij, "Effect of Soret diffusion on lean hydrogen/air flames at normal and elevated pressure and temperature," *Combust. Theory Model.*, vol. 21, no. 5, pp. 879–896, 2017, doi: 10.1080/13647830.2017.1311028.
- [21] Z. Y. Sun, F. S. Liu, X. C. Bao, and X. H. Liu, "Research

on cellular instabilities in outwardly propagating spherical hydrogen-air flames,” *Int. J. Hydrogen Energy*, vol. 37, no. 9, pp. 7889–7899, 2012, doi: 10.1016/j.ijhydene.2012.02.011.

- [22] “Tian et al. - 2022 - The Effects of Turbulence on the flame Structure and No Formation of Ammonia Turbulent Premixed Combustion at Various.pdf.”
- [23] S. Kadowaki, “The influence of hydrodynamic instability on the structure of cellular flames Comment on ‘The influence of hydrodynamic instability on the structure of cellular flames’ The influence of hydrodynamic instability on the structure of cellular flames,” *Phys. Fluids*, vol. 11, p. 2024, 1999, doi: 10.1063/1.870201.

APPENDIX

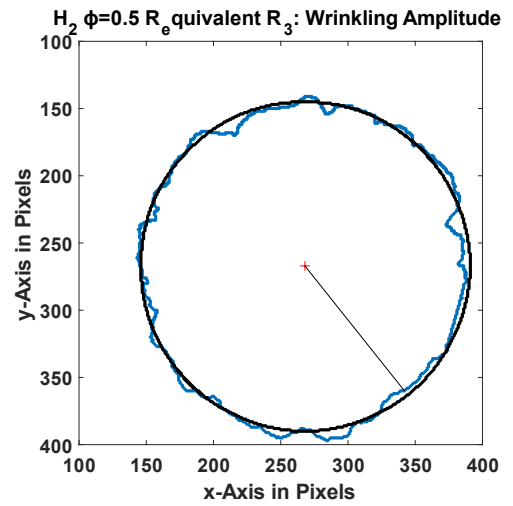
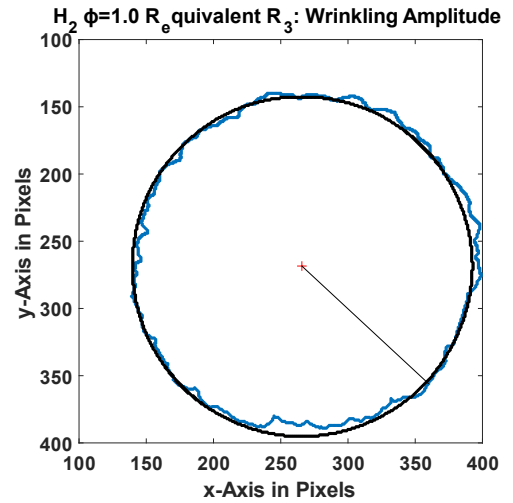
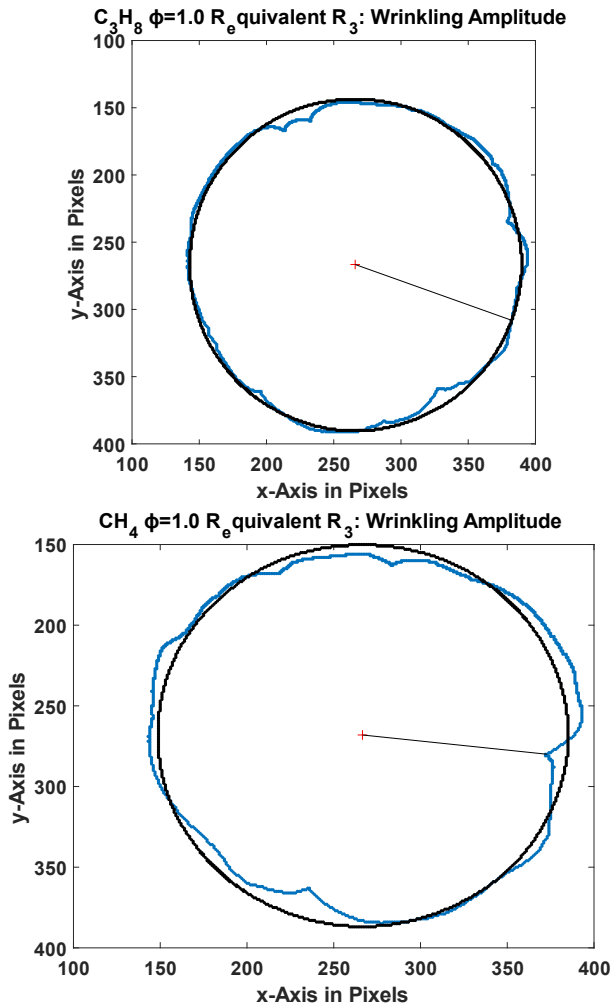
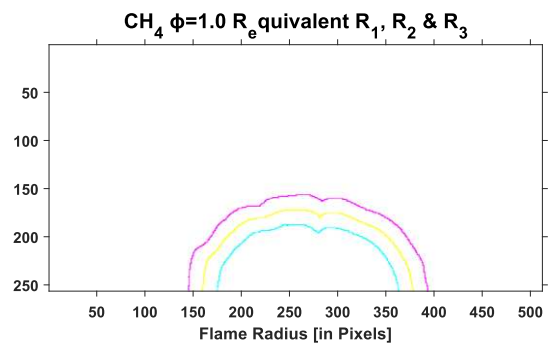


FIGURE A1: Flame Contours



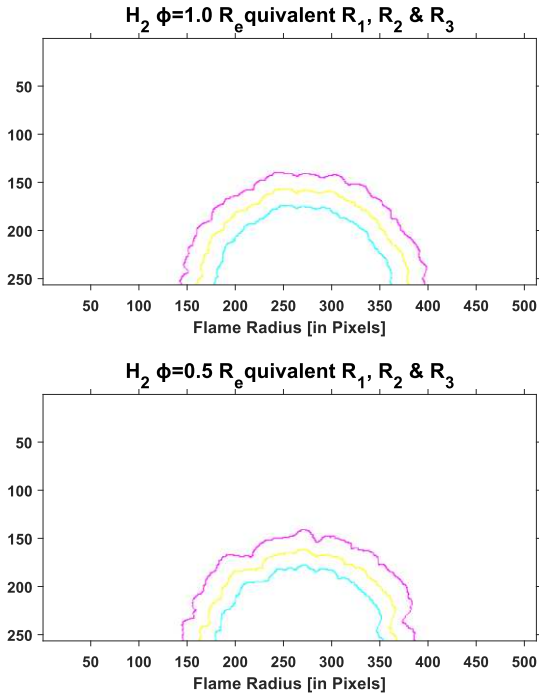


FIGURE A2: Wrinkling Diagram

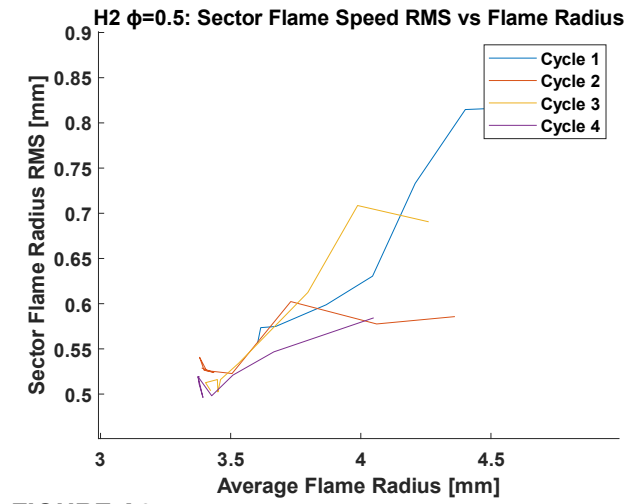
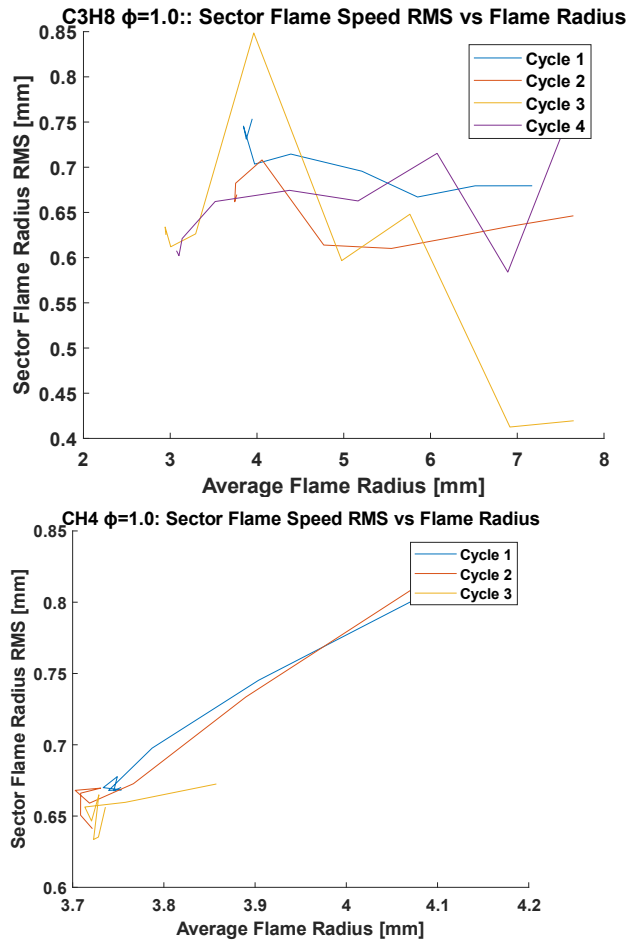


FIGURE A3: Sector Flame Speed RMS

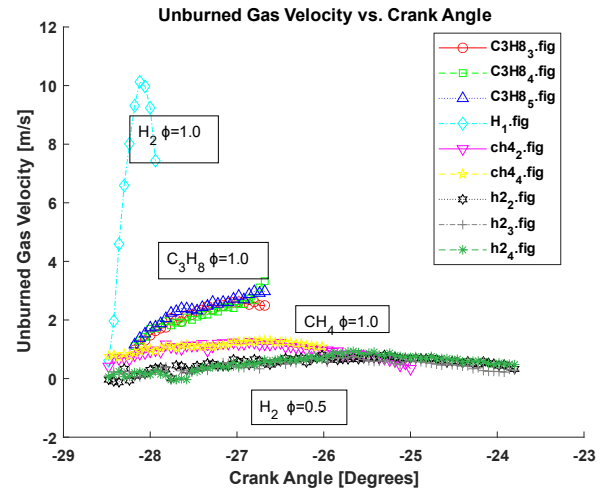


FIGURE A4: Unburned Gas Velocities

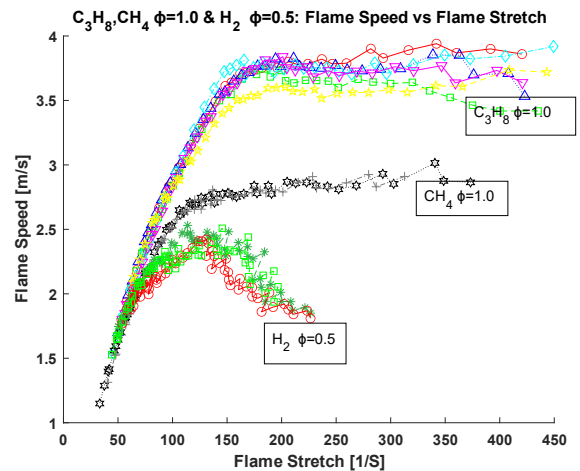


FIGURE A5: Flame Speed vs. Flame Stretch

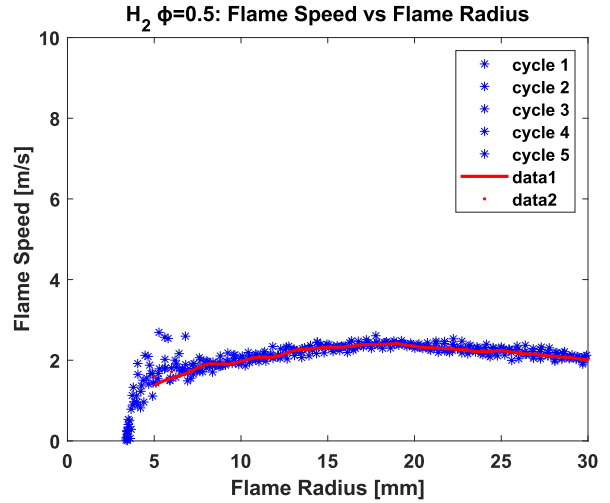
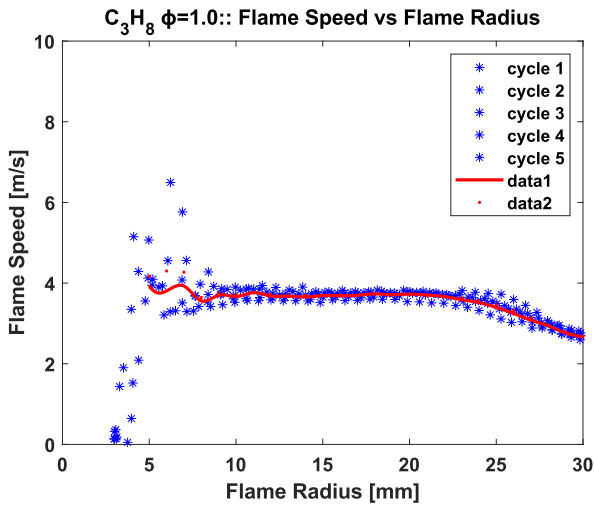


FIGURE A5: Flame Speed vs. Flame Radius

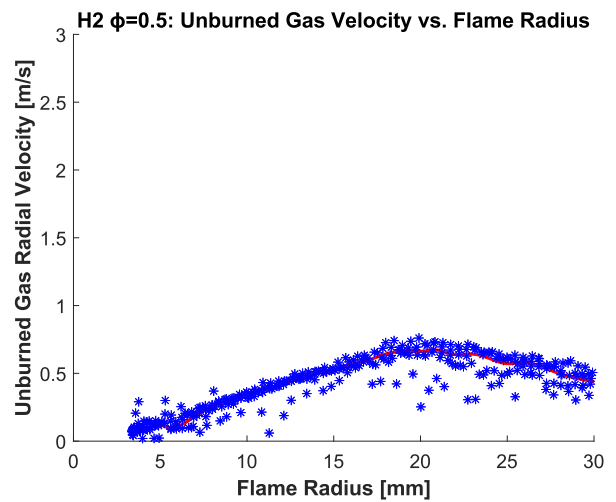
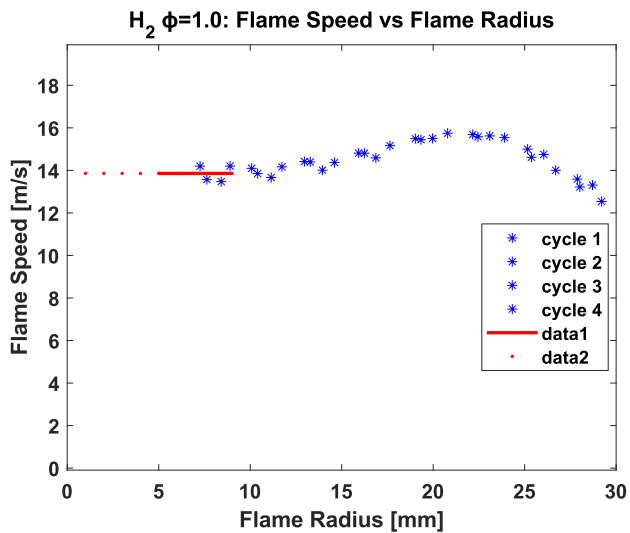
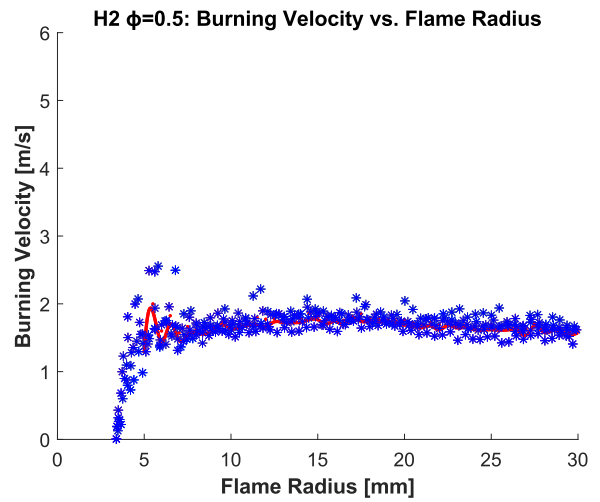
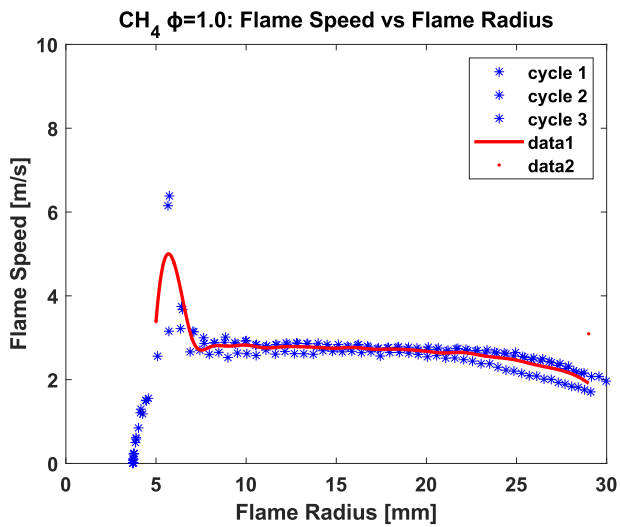


FIGURE A6: Burning Velocity & Unburned Gas Vel: $H_2 \phi=0.5$